Direct Numerical Simulation of Hypersonic Turbulent Boundary Layer inside an Axisymmetric Nozzle

Junji Huang* , Chao Zhang* and Lian Duan†

Missouri University of Science and Technology, Rolla, MO 65409

Meelan M. Choudhari‡

NASA Langley Research Center, Hampton, VA 23681

As a first step toward a study of acoustic disturbance field within a conventional, hypersonic wind tunnel, direct numerical simulations (DNS) of a Mach 6 turbulent boundary layer on the inner wall of a straight axisymmetric nozzle are conducted and the results are compared with those for a flat plate. The DNS results for a nozzle radius to boundary-layer thickness ratio of 5.5 show that the turbulence statistics of the nozzle-wall boundary layer are nearly unaffected by the transverse curvature of the nozzle wall. Before the acoustic waves emanating from different parts of the nozzle surface can interfere with each other and undergo reflections from adjacent portions of the nozzle surface, the rms pressure fluctuation beyond the boundary layer edge increases toward the nozzle axis, apparently due to a focusing effect inside the axisymmetric configuration. Spectral analysis of pressure fluctuations at both the wall and the freestream indicates a similar distribution of energy content for both the nozzle and the flat plate, with the peak of the premultiplied frequency spectrum at a frequency of $\omega\delta/U_\infty \approx 6.0$ inside the free stream and at $\omega\delta/U_\infty \approx 2.0$ along the wall. The present results provide the basis for follow-on simulations involving reverberation effects inside the nozzle.

Nomenclature

C_p	heat capacity at constant pressure, J/(K·kg)
C_v	heat capacity at constant volume, J/(K·kg)
H	shape factor, $H = \delta^*/\theta$, dimensionless
M	Mach number, dimensionless
Pr	Prandtl number, $Pr = 0.71$, dimensionless
R	ideal gas constant, $R = 287$, J/(K·kg), or radius of the axisymmetric nozzle, m
Re_θ	Reynolds number based on momentum thickness and freestream viscosity, $Re_\theta \equiv \frac{\rho_\infty U_\infty \theta}{\mu_\infty}$, dimensionless
Re_{δ_2}	Reynolds number based on momentum thickness and wall viscosity, $Re_{\delta_2} \equiv \frac{\rho_\infty U_\infty \theta}{\mu_w}$, dimensionless
Re_τ	Reynolds number based on shear velocity and wall viscosity, $Re_\tau \equiv \frac{\rho_w u_\tau \delta}{\mu_w}$, dimensionless
rms	root mean square
T	temperature, K
T_r	recovery temperature, $T_r = T_\infty(1 + 0.9\frac{\gamma-1}{2}M_\infty^2)$, K
U_∞	freestream velocity, m/s
a	speed of sound, m/s
p	pressure, Pa
q	dynamic pressure, Pa
r	radial coordinate
u	streamwise velocity, m/s

*Graduate Student, Student Member, AIAA

†Assistant Professor, Senior Member, AIAA

‡Aerospace Technologist, Computational AeroSciences Branch, M.S. 128. Associate Fellow, AIAA

American Institute of Aeronautics and Astronautics

u_τ	friction velocity, m/s
v	spanwise velocity, m/s
w	wall-normal velocity, m/s
x	streamwise direction of the right-hand Cartesian coordinate
y	spanwise direction of the right-hand Cartesian coordinate
z	wall-normal direction of the right-hand Cartesian coordinate
z_τ	viscous length, $z_\tau = \nu_w/u_\tau$, m
γ	specific heat ratio, $\gamma = C_p/C_v$, dimensionless
δ	boundary layer thickness, m
δ^*	displacement thickness, $\delta^* = \int_{R-3\delta}^{R} \frac{r}{R}\left(1 - \frac{\rho u}{\rho_\infty U_\infty}\right)dr$, m
θ	momentum thickness, $\theta = \int_{R-3\delta}^{R} \frac{r}{R}\frac{\rho u}{\rho_\infty U_\infty}\left(1 - \frac{u}{U_\infty}\right)dr$, m
κ	thermal conductivity, $\kappa = \mu C_p/Pr$, W/(m·K)
μ	dynamic viscosity, $\mu = 1.458 \times 10^{-6}\frac{T^{3/2}}{T+110.4}$, kg/(m·s)
ν	kinematic viscosity, $\nu = \mu/\rho$, m²·s
ρ	density, kg/m³

Subscripts

i	inflow station for the domain of direct numerical simulations
rms	root mean square
w	wall variables
∞	freestream variables
t	stagnation quantities

Superscripts

$+$	inner wall units
$\overline{(\cdot)}$	averaged variables
$(\cdot)'$	perturbation from averaged variable

I. Introduction

The elevated freestream disturbance levels in conventional (i.e., noisy) high-speed wind tunnels usually result in an earlier onset of transition relative to that in a flight environment or in a quiet tunnel. Yet, the conventional facilities continue to be used for transition sensitive measurements because of the size and Reynolds number limitations of existing quiet facilities and the prohibitive cost of flight tests. To enable a better use of transition data from the conventional facilities, it is important to understand the acoustic fluctuation field that dominates the freestream disturbance environment in those facilities. With increased knowledge of the receptivity mechanisms of high-speed boundary layers,[1,2] it becomes particularly important to characterize the details of the tunnel acoustics originating from the tunnel-wall turbulent boundary layers.

Direct numerical simulations (DNS) of the acoustic fluctuation field radiated from tunnel-wall turbulent boundary layers can overcome a number of difficulties encountered during experimental measurements of tunnel freestream disturbances and also provide access to quantities that cannot be measured easily.[3–5] Successful application of DNS for capturing the freestream acoustic pressure fluctuations has been demonstrated for spatially-developing turbulent boundary layers over a flat plate at Mach 2.5, 6, and 14.[6–8] These flat-plate simulations have the benefits of isolating more easily the acoustic radiation from a single surface, thus facilitating a comprehensive understanding of the freestream disturbance field and its dependence on boundary-layer parameters (e.g., freestream Mach number, wall temperature, Reynolds number). Most hypersonic wind tunnels are, however, axisymmetric. As a result, the freestream disturbances in the tunnel environment reflect the combined outcome of acoustic radiation from all regions of the tunnel wall. The present study is motivated by the need to help enable practical applications of the simulation data for freestream disturbances in the context of actual wind-tunnel experiments and to guide the measurement of tunnel disturbances in high-speed facilities. To simulate the acoustic radiation within an enclosed environment while simultaneously facilitating a direct comparison with acoustic radiation from a single flat wall in an unconfined setting, this paper focuses on investigating the effects of a cylindrical test section on the interior noise field. An attempt will also be made to understand where the previous flat-plate acoustic

American Institute of Aeronautics and Astronautics

simulations are applicable; and where, if at all, the effects of an axisymmetric enclosure on the noise field need to be taken into account.

The paper is structured as follows. The flow conditions and numerical methods are outlined in Section II. Section III presents comparisons of the turbulent and acoustic statistics between the turbulent boundary layer on the nozzle wall and that on a flat plate. A summary of the overall findings is given in Section IV.

II.   Flow Conditions and Numerical Methodology

Freestream conditions used in the DNS set up are summarized in Table 1, which fall within the range of nozzle exit conditions of the Purdue Mach 6 Quiet Tunnel (BAM6QT).[5,9] The wall temperature is 300 K, corresponding to a wall-to-recovery temperature ratio of $T_w/T_r \approx 0.76$. To simulate the acoustic radiation within an enclosed environment while simultaneously facilitating a direct comparison with acoustic radiation from a single flat wall in an unconfined setting, we consider a hypothetical straight nozzle with a cylindrical shape. By choosing a cylindrical geometry, the effects of surface curvature and pressure gradient in the streamwise direction can be neglected to the leading order, thus avoiding extraneous complexity in the simulation. Under the chosen flow condition, the ratio of the tunnel radius to the tunnel-wall boundary-layer thickness at the inlet is $R/\delta \approx 10.5$, and becomes about 5.5 at the outlet. The modest value of R/δ also makes it numerically affordable to propagate high-frequency acoustic waves over large axial distances while at the same time guarantees that the transverse curvature of the cylindrical wall has a negligible influence on the boundary-layer profiles.

Table 1.   Nominal freestream conditions for the DNS of a Mach 6 turbulent boundary layer.

Cases	M_∞	U_∞ (m/s)	ρ_∞ (kg/m³)	T_∞ (K)	δ_i (mm)
CylinderExpand	5.73	868.0	0.047	57.1	7.1
FlatPlate	5.97	873.2	0.044	53.2	10.4

A.   Governing Equations and Numerical Methods

The working fluid is assumed to be a perfect gas and the usual constitutive relations for a Newtonian fluid are used: the viscous stress tensor is linearly related to the rate-of-strain tensor, and the heat flux vector is linearly related to the temperature gradient through Fourier's law. The coefficient of viscosity μ is computed from Sutherlands's law, and the coefficient of thermal conductivity κ is computed from $\kappa = \mu C_p/Pr$, with the molecular Prandtl number $Pr = 0.71$. A detailed description of the governing equations can be found in Wu et al.[10]

The full three-dimensional compressible Navier-Stokes equations are solved numerically either in cylindrical coordinates (case CylinderExpand) or in curvilinear Cartesian coordinates (case FlatPlate). For cylinder cases, the governing flow equations are solved with a collocated grid, hence a solution point exists at the polar axis ($r = 0$). The singularities arising at the polar axis due to the $1/r$ term in the governing flow equations are handled by using a technique based on series expansions,[11] which has been shown to enable the computation of nonaxisymmetric flows in cylindrical coordinates using highly accurate finite-difference schemes on nonstaggered grids. The method of Bogey[12] is used to avoid the time-step restriction due to the fine grid spacing in the azimuthal direction near the centerline.

The inviscid fluxes of the governing equations are computed using a seventh-order weighted essentially non-oscillatory (WENO) scheme. Compared with the original finite-difference WENO introduced by Jiang and Shu,[13] the present scheme is optimized by means of limiters[10,14] to reduce the numerical dissipation. Both an absolute limiter on the WENO smoothness measurement and a relative limiter on the total variation are employed simultaneously during the simulation. The viscous fluxes are discretized using a fourth-order central difference scheme and time integration is performed using a third-order low-storage Runge-Kutta scheme.[15]

The details of the DNS methodology have been documented in our previous simulations of acoustic radiation by turbulent boundary layers.[6–8] The DNS solver has been previously shown to be suitable for computing transitional and fully turbulent flows, including hypersonic turbulent boundary layers,[16,17] the

American Institute of Aeronautics and Astronautics

propagation of linear instability waves in 2D high-speed boundary layers, and secondary instability and laminar breakdown of swept-wing boundary layers.[18,19]

B. Simulation Setup and Boundary Conditions

Table 2 shows the turbulent boundary layer properties for Case CylinderExpand and FlatPlate. Geometry and grid information are summarized in Table 3 for the current DNS cases. For Case CylinderExpand, the mesh geometry is represented in the cylindrical system, as is shown in Figure 1, with x being the streamwise direction, r the radial direction, and θ the azimuthal direction. The radius of the nozzle is 10.6 δ_i and the length along the axial direction is about 71.3 δ_i, where $\delta_i = 0.071$ m is the inlet boundary layer thickness. Two slightly different cylinders are considered here, one corresponding to a straight nozzle with a constant radius, and the other with a slightly increasing radius to account for the boundary layer growth in the downstream direction. The bottom left of Figure 1 shows the image of a straight nozzle without expansion, and the right figure shows a conical nozzle with an expansion angle of 0.39°, which was estimated from the growth rate of displacement thickness along a flat plate under the same freestream condition. Grid dimensions used in both simulations are $1000 \times 960 \times 364$ in the streamwise, azimuthal and radial directions, respectively. Uniform mesh distributions are used in both streamwise and azimuthal directions. Based on the viscous length scale $z_\tau = 46.0$ μm at $x/\delta_i = 50$, the value of constant streamwise grid spacing is 11.0, and azimuthal grid spacing on nozzle wall is 10.8. Grid distribution in the radial direction is clustered near wall with a near-wall grid spacing of $\Delta r^+ = 0.58$, and is kept uniform in the freestream ($\Delta r^+ = 6.1$) up to approximately 6.0 δ, where δ is the local mean boundary layer thickness at $x/\delta_i = 50$. The above grid distribution ensures that both boundary layer and freestream region are well resolved in the current simulation. Note that the reference value and above estimates of grid spacings are evaluated at $x/\delta_i = 50$ from the cylinder inlet.

Table 2. Boundary layer properties at the station selected for the analysis of the turbulence field ($x/\delta_i = 50.0$).

Case	T_w (K)	T_w/T_r	Re_θ	Re_τ	$Re_{\delta 2}$	θ (mm)	H	δ (mm)	z_τ (μm)	u_τ (m/s)
CylinderExpand	300	0.76	4968.4	254.2	1035.5	0.45	14.4	11.7	46.0	44.8
FlatPlate	300	0.76	7530.6	326.6	1411.3	0.67	14.6	17.0	51.7	45.7

Table 3. Grid resolution and domain size for the axisymmetric nozzle (case CylinderExpand) and flat plate (case FlatPlate). Grid resolutions are normalized by the viscous length scale z_τ at $x/\delta_i = 50.0$. Δz^+_{min} and Δz^+_{max} are the minimum and maximum wall-normal grid spacing for $0 \leq (R-r)/\delta \leq 6.0$ (CylinderExpand) or $0 \leq (R-r)/\delta \leq 4.2$ (FlatPlate) at $x/\delta_i = 50.0$.

Cases	$N_x \times N_y$ $(N_\theta) \times N_z$ (N_r)	L_x/δ_i	L_y/δ_i	L_z/δ_i (R/δ_i)	Δx^+	Δy^+ (wall)	Δz^+_{min} (Δr^+_{min})	Δz^+_{max} (Δr^+_{max})
CylinderExpand	$1000 \times 960 \times 364$	71.3	–	10.6	11.0	10.7	0.58	6.1
FlatPlate	$1920 \times 320 \times 500$	93.5	8.3	52.7	9.8	5.2	0.52	5.4

For Case FlatPlate, the domain size is ($93.5\,\delta_i, 8.3\,\delta_i, 52.7\,\delta_i$) in the streamwise, spanwise and wall-normal directions, respectively, where $\delta_i = 0.0104$ m represents the mean boundary layer thickness specified at the inlet of flat plate. The grid points are uniformly spaced in the streamwise and spanwise directions with grid spacings of $\Delta x^+ = 9.8$ and $\Delta y^+ = 5.2$, respectively. The grids in the wall-normal direction are clustered in the boundary layer with $\Delta z^+ = 0.52$ at the wall, and kept uniform in the free stream ($\Delta z^+ = 5.4$) up to approximately 4.2 δ, where δ is the local mean boundary-layer thickness at $x/\delta_i = 50$. The number of grid points for Case FlatPlate in the streamwise, spanwise, and wall-normal directions are 1920, 320 and 500, respectively. Grid resolutions are evaluated by viscous length at $x/\delta_i = 50$.

For the inlet boundary condition, a newly implemented digital-filtering (DF) based method[20,21] is applied to generate inflow turbulent flow for both cylinder and flat plate cases, with the mean boundary-layer profiles and the Reynolds stress tensor at the inflow extracted from a RANS simulation for each case. The adequacy of the DF inflow method for predicting the global pressure field induced by hypersonic turbulent boundary layers is demonstrated by comparing the pressure statistics downstream of the inflow adjustment region with
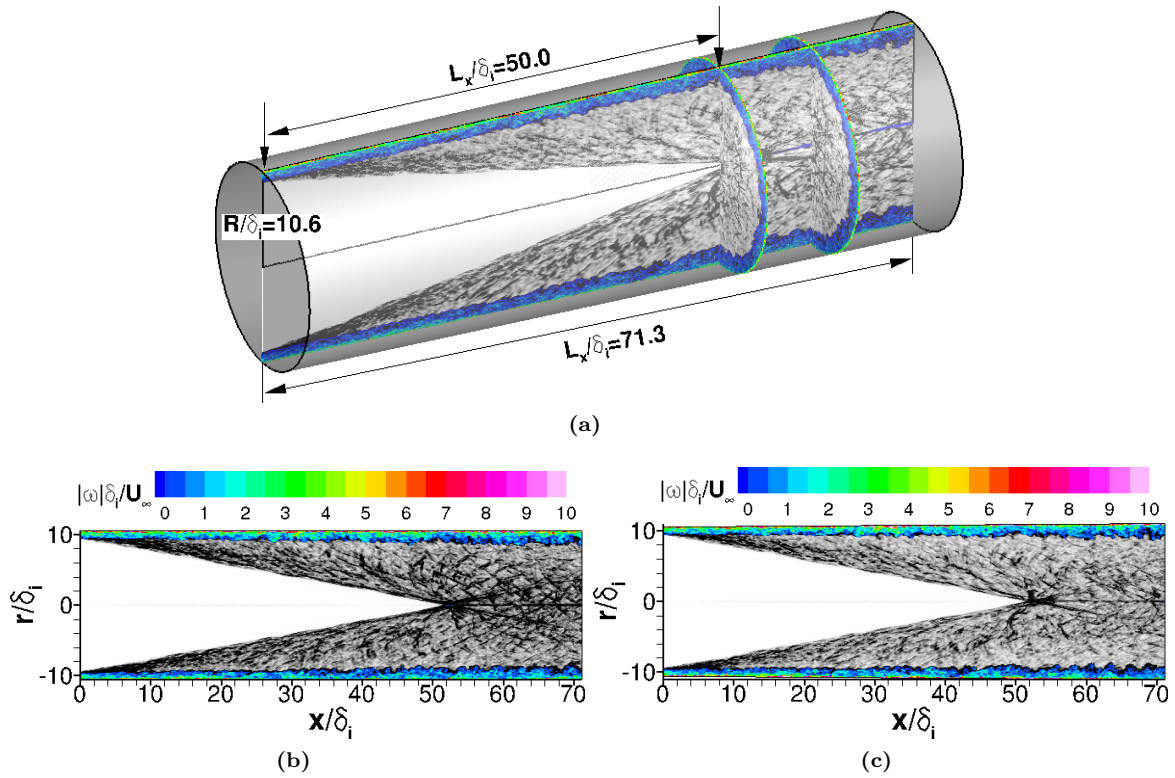
(a)

(b)

(c)

Figure 1. **(a): Numerical schlieren image of computational domain and simulation setup for Case CylinderExpand; two-dimensional numerical schlieren images of (b): a straight nozzle and (c): a conical nozzle with an expanding angle of** $0.39°$ **in a streamwise wall-normal plane. Contours are colored by the magnitude of vorticity.**

those predicted by a rescaling-recycling (RR) inflow method[6] as illustrated in Figure 2. For our follow-on study of acoustic fluctuations in convergent-divergent nozzle geometries typical of a hypersonic wind tunnel, the DF-based inflow method is required, given that the RR-based method requires an equilibrium region to invoke scaling arguments and is limited to flat-plate or straight-pipe like geometries.

On the nozzle wall, no-slip conditions are applied for the three velocity components and an isothermal condition is used for the temperature, with $T_w \approx 0.76T_r$. At the outlet boundary, unsteady nonreflecting boundary conditions based on Thompson[22] are imposed. Centerline treatment of Constantinescu[11] is used at the polar axis to remove singularities in the radial direction, and Bogey[12] in the azimuthal direction to alleviate the time-step limitation near the centerline. For the inlet boundary condition, a DF-based method[20, 21] is applied to generate synthetic turbulent flow for both cylinder and flat plate cases. This ensures a direct comparison of the two turbulent boundary layers despite their different geometries. The method is modified by the use of change-of-basis transformation for second-order tensors on curvilinear nonuniform grid. In particular, the digital filtering operation is carried out only in a zone within the boundary layer. The rest of the inflow plane is imposed with the prescribed mean flow variables. The thickness of this zone corresponds to the region between the wall and the inlet boundary layer thickness. The mean velocity, pressure, temperature and Reynolds stress tensor (which is required by the digital-filter method) are obtained from a separate RANS simulation of the same configuration under the same flow conditions, as is done in our previous simulation.[23]
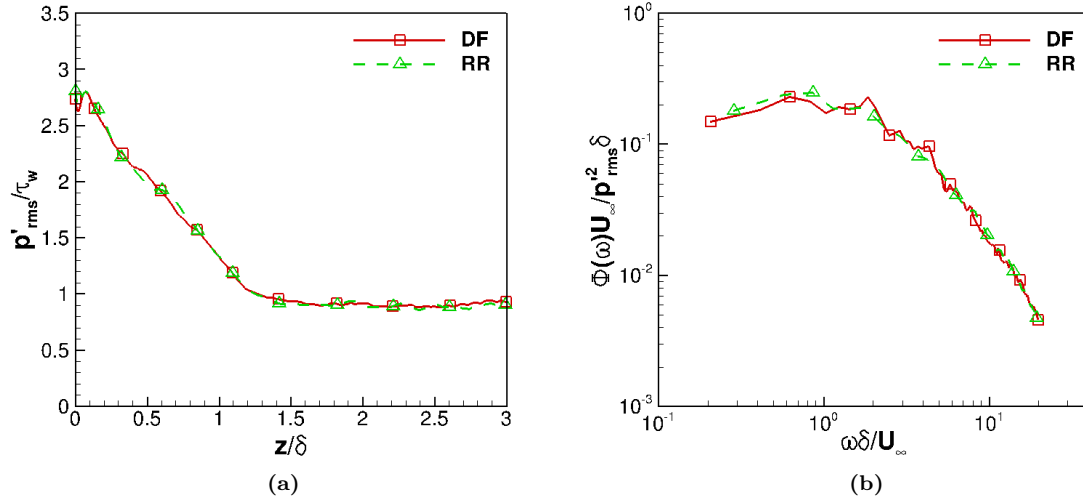

Figure 2. The effect of turbulent inflow generation method on rms pressure fluctuation. (a) The rms pressure fluctuation profile at the selected streamwise location corresponding to $Re_\tau \approx 400$; (b) Normalized frequency spectrum of computed pressure signal at $z/\delta = 2.31$. The pressure spectrum is normalized so that the area under each curve is equal to unity. DF: digital filtering method; RR: rescaling and recycling method.

III.   Results

In this section, DNS results for the nozzle-wall turbulent boundary layer are presented and compared with those for the flat plate.

Figure 3a plots the streamwise distribution of the mean pressure coefficient for various DNS cases. For Case CylinderExpand, the growth of the turbulent boundary layer on the inner surface of the nozzle has been accounted for by expanding the nozzle subtly via a streamwise expansion angle of 0.39°. A turbulent boundary layer with nearly zero streamwise pressure gradient is maintained between $20 < x/\delta_i < 70$ that enables a direct comparison with the DNS results of zero-pressure-gradient hypersonic turbulent boundary layer over a flat plate. Figure 3b further shows that the skin friction of Case CylinderExpand matches that of Case FlatPlate for $x/\delta_i > 30$. For all DNS cases, the rms pressure fluctuation signal becomes homogeneous

American Institute of Aeronautics and Astronautics

in the streamwise direction for $x/\delta_i > 35$ as shown in Figure 4.

Figure 5a shows the streamwise evolution of the Karman number Re_τ. It should be noted that the inflow profile chosen for Case CylinderExpand is extracted from a relatively more upstream location of the RANS results to avoid an earlier shock incident (as seen from Figure 1) from the opposite nozzle wall. Therefore, the inflow profiles in these two DNS cases are different, i.e., $\delta_i = 7.1$ mm for Case CylinderExpand but $\delta_i = 10.4$ mm for Case FlatPlate, the absolute value of the Karman number differs at the same x/δ_i locations between the flat-plate and nozzle boundary layers. However, they both grow with the same rate along the streamwise direction. The integral parameters nearly collapse between the flat-plate and nozzle-wall boundary layers after normalizing each measure of boundary-layer thickness as shown in Figures 5b, 5c, 5d. For the axisymmetric boundary layer, the displacement thickness δ^* and the momentum thickness θ are defined, respectively, as

$$\delta^* = \int_{R-3\delta}^{R} \frac{r}{R} \left(1 - \frac{\bar{\rho}\bar{u}}{\rho_\infty U_\infty} \right) dr \tag{1}$$

$$\theta = \int_{R-3\delta}^{R} \frac{r}{R} \frac{\bar{\rho}\bar{u}}{\rho_\infty U_\infty} \left(1 - \frac{\bar{u}}{U_\infty} \right) dr \tag{2}$$

The above definitions are derived based on those of Eggels[24] by assuming $R >> \delta^*$ and $R >> \theta$.

The van Driest transformed mean streamwise velocity profiles for the DNS cases are shown in Figure 6. The mean velocity conforms well to the incompressible law-of-wall. Both the flat-plate and nozzle cases show a narrow logarithmic region. The van Driest transformed mean deficit velocity agrees well between both cases.

Figure 7 shows the normalized rms pressure fluctuation p'_{rms}/τ_w as a function of wall-normal distance. While the rms of pressure asymptotes to a constant value in the free stream for the flat-plate case, it increases continuously toward the center of the nozzle for the nozzle case (Figure 7a). The increase in p'_{rms}/τ_w toward the center region for the nozzle case is caused by the focusing effect due to the axisymmetric geometry. Such a geometry dependence needs further study in future simulations.

The bulk propagation speed (U_b), defined as the value that minimizes the difference between the real time evolution of $p(x,t)$ and a frozen wave $p(x - U_b t)$,[6, 25] is plotted as a function of the wall-normal coordinate in Figure 8. The bulk propagation speed of the pressure structures is insensitive to the effect of axisymmetry. For both cases, the bulk propagation speed outside the boundary layer is significantly smaller than the freestream velocity and approaches a value of approximately $0.7U_\infty$.

The normalized frequency spectra of computed pressure signals at wall and freestream locations for Case CylinderExpand nearly overlaps that of FlatPlate, as shown in Figure 9. The slight difference at high frequencies may be due to the relatively coarse spanwise resolution of Case CylinderExpand ($\Delta y^+ \approx 11$) in comparison with that of Case FlatPlate ($\Delta y^+ \approx 5.2$). The low frequency portions of the spectra in Case CylinderExpand are not well resolved because of the limited length of sampling from that simulation. Figure 10a shows the premultiplied pressure spectra[25] at various heights above the wall surface for Case CylinderExpand. The peak of the spectrum in the inner boundary layer is centered on $\omega\delta/U_\infty \approx 6$. As one moves to the freestream, the peak is centered at a lower frequency, $\omega\delta/U_\infty \approx 2$. Figure 10b shows the comparison of the premultiplied spectra between Case CylinderExpand and FlatPlate. The magnitudes of spectral peaks and the corresponding frequencies collapse between the two cases at both wall and freestream locations.

Figures 11, 12, and 13 display the contours of two-point correlations at multiple wall-normal lcoations. The good agreement between the FlatPlate and CylinderExpand cases can be seen at all heights, indicating that the spatial structure of the boundary-layer-induced pressure fluctuations is relatively insensitive to transverse curvature of the surface.

Finally, numerical schlieren images of the radiated acoustic fields are shown in Figure 14. The wave fronts exhibit a preferred orientation within the streamwise-radial plane (Figure 14a), very similar to that seen for the flat plate turbulent boundary layer.[6–8]

IV.   Summary

Direct numerical simulation of a zero-pressure-gradient spatially-developing turbulent boundary layer inside an axisymmetric straight nozzle is conducted and compared with that on a flat plate. The freestream
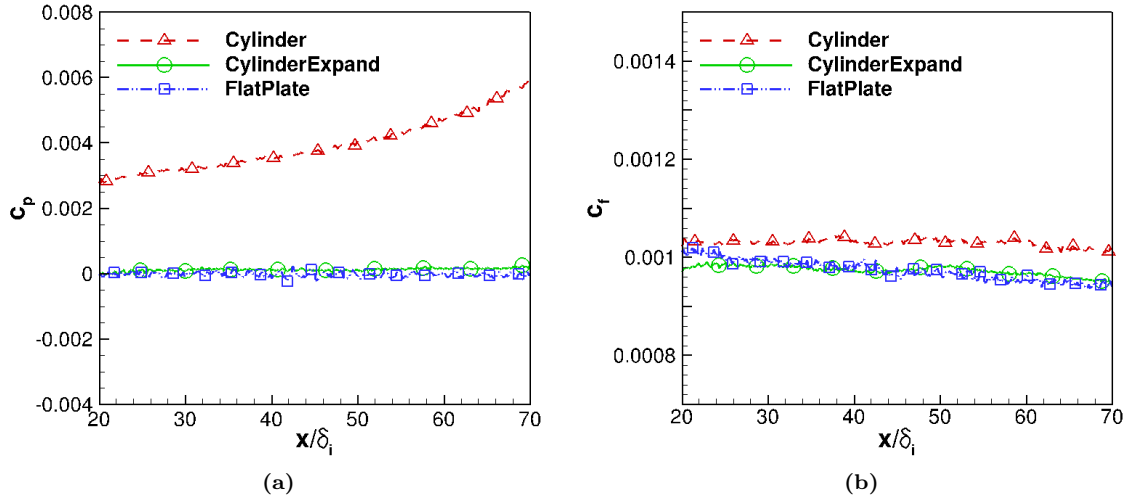
Figure 3. Streamwise distribution of (a) the mean wall pressure coefficient, $c_p = (p_w - p_\infty)/q_\infty$; (b) skin friction coefficient along wall.
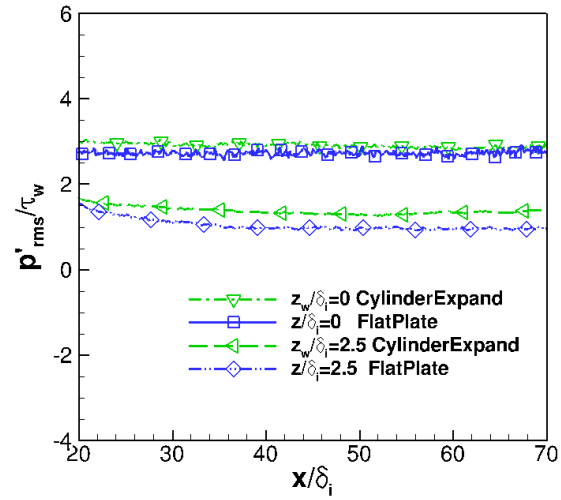

Figure 4. Streamwise distribution of normalized rms turbulence fluctuation in the downstream portion of the computational domain $(20 < x/\delta_i < 70)$. Wall $(z/\delta_i = 0)$ and freestream location $(z/\delta_i = 2.5)$ are shown in (b).
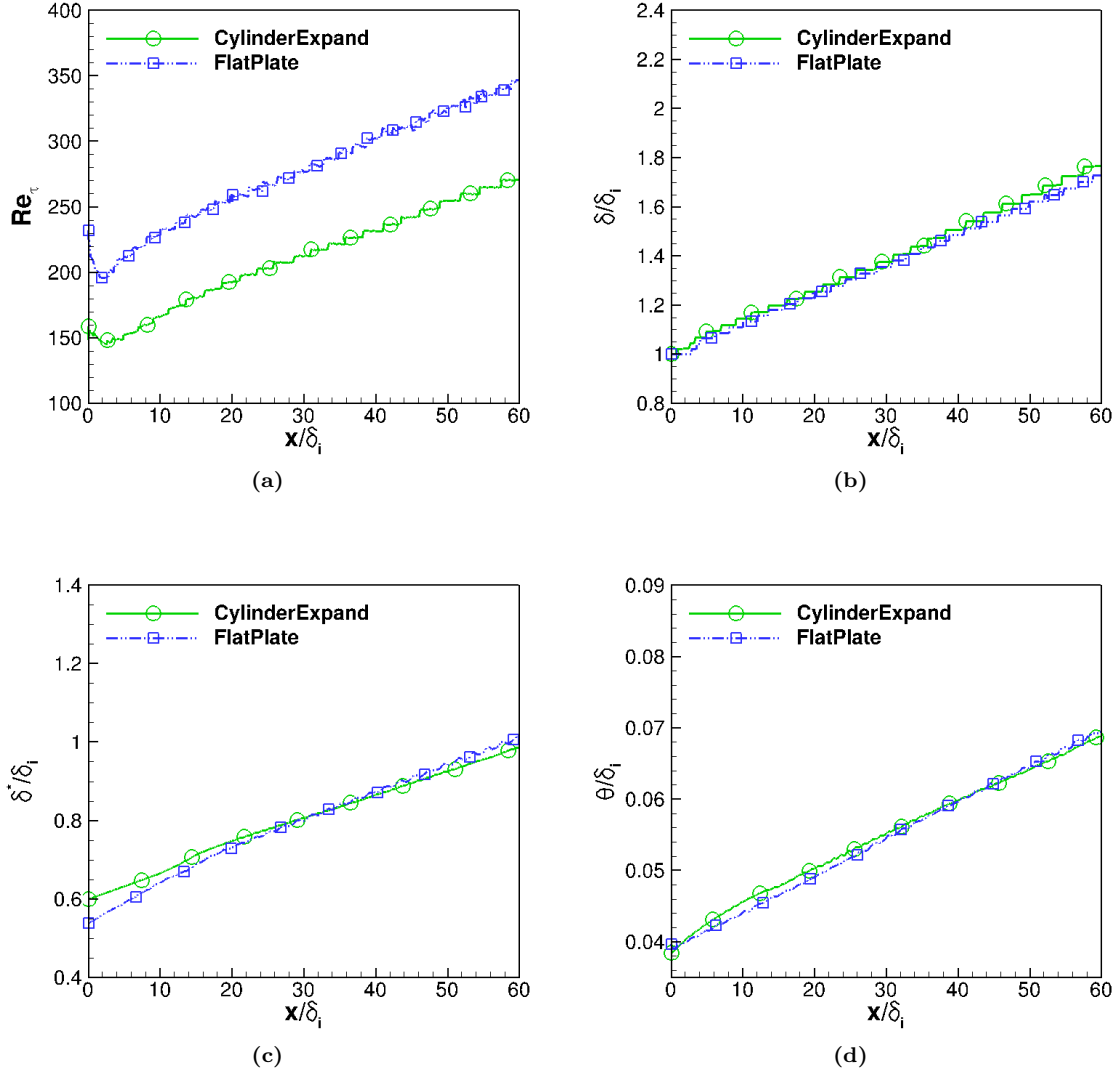
American Institute of Aeronautics and Astronautics

Figure 5. Streamwise evolution of boundary-layer properties (a) Karman number Re_τ; (b) normalized boundary-layer thickness; (c) normalized displacement thickness; (d) normalized momentum thickness.

American Institute of Aeronautics and Astronautics
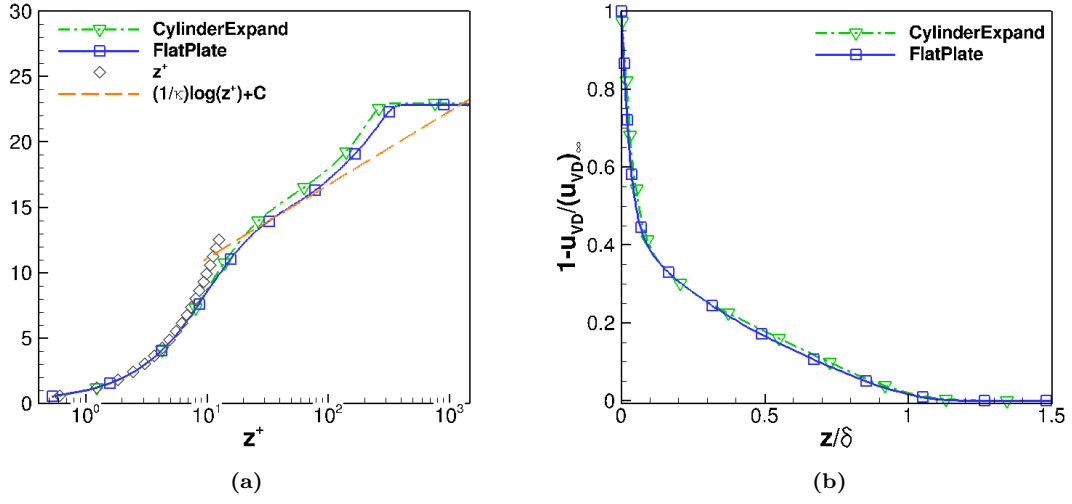
Figure 6. (a) van Driest transformed mean velocity profile ($\kappa = 0.41, C = 5.5$) (b) van Driest transformed mean deficit velocity at $x/\delta_i = 50$.
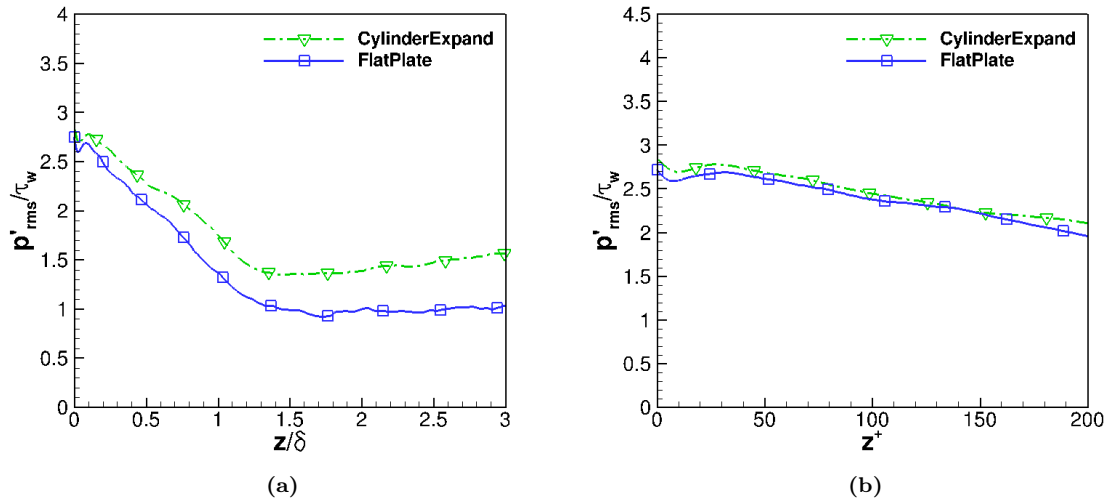
Figure 7. The rms pressure fluctuation profile at selected streamwise location corresponding to $Re_\tau \approx 300$ in (a) outer and (b) inner units
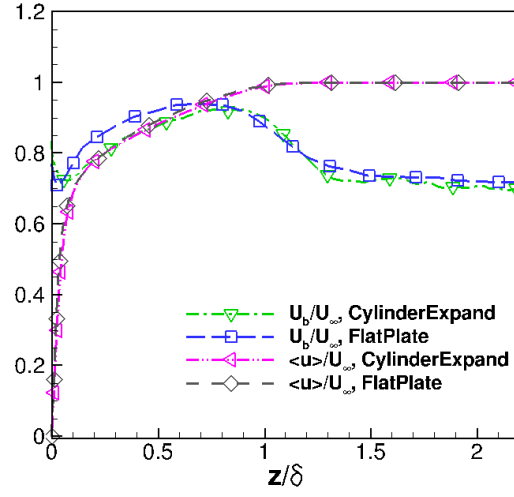
Figure 8. Bulk propagation speed of pressure fluctuations as a function of wall-normal distance at $x/\delta_i = 50$.
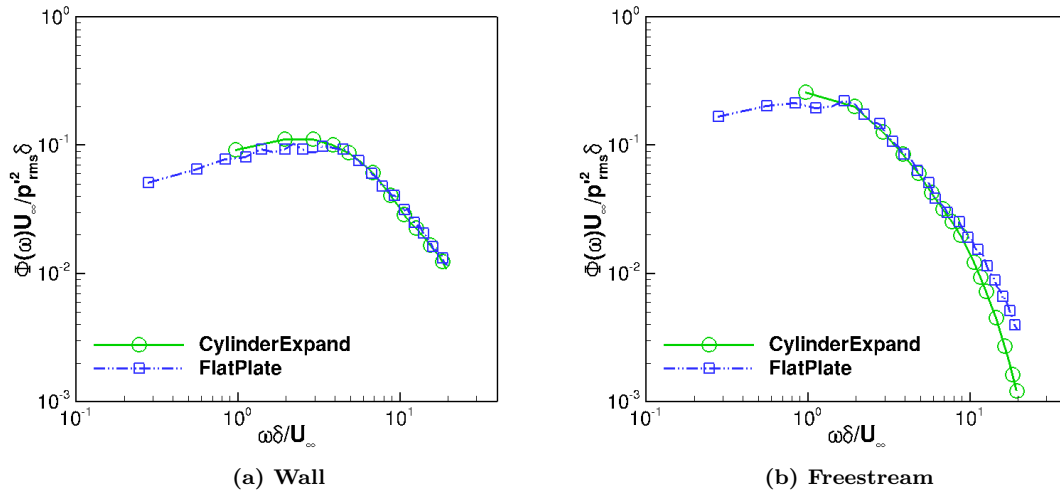

(a) Wall

(b) Freestream

Figure 9. Normalized frequency spectrum of computed pressure signal at selected heights for Case CylinderExpand and FlatPlate. The freestream are taken at $(R-r)/\delta = 2.12$ for Case CylinderExpand and $z/\delta = 2.2$ for Case FlatPlate. The pressure spectrum is normalized so that the area under each curve is equal to unity.
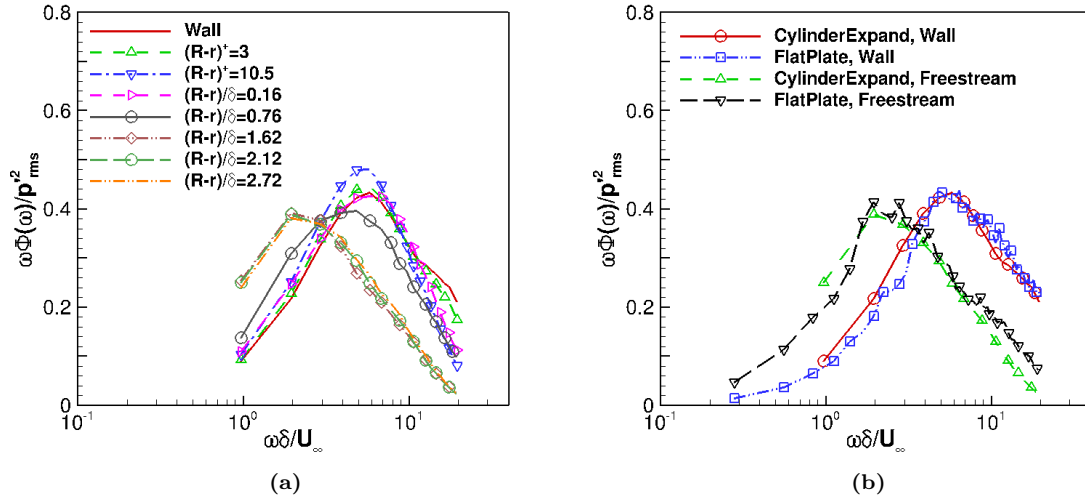
Figure 10. Pre-multiplied power spectrum of pressure signals (a) at selected heights for Case CylinderExpand; (b) comparison between Case CylinderExpand and FlatPlate. The freestream are taken at $(R-r)/\delta = 2.12$ for Case CylinderExpand and $z/\delta = 2.2$ for Case FlatPlate. The pressure spectrum is normalized so that the area under each curve is equal to unity. $(R-r)^+ = (R-r)/z_\tau$.

conditions of both surface geometries correspond to those at the nozzle exit of the BAM6QT facility at Purdue University when the latter is operated under noisy-flow runs. The growth of the turbulent boundary layer on the nozzle wall is accommodated for via a tiny, conical expansion of nozzle radius in the streamwise direction. The simulations show that turbulent statistics within the boundary layer are insensitive to the transverse curvature of the wall for $R/\delta \approx 5.5$ (nozzle exit). For both the nozzle and flat plate, spectral analysis shows a similar frequency content of pressure fluctuations and two-point spatial correlation indicates a similar orientation of large-scale pressure structures with respect to the flow direction. The rms pressure fluctuation increases toward the center of the nozzle, as against the constant valued asymptote for the flat plate case. The effect of axisymmetric geometry on the freestream acoustic radiation needs further study in future simulations, especially in the farther downstream region where the acoustic waves have reached the other parts of the nozzle surface, such that the acoustic field near the axis consists of both direct radiation and secondary and tertiary reflections, etc.

The study may suggest that, before the acoustic waves emanating from any given portion of the tunnel wall interfere with the waves originating from the other side of the nozzle wall, the tunnel noise in a large-scale conventional hypersonic wind tunnel with an axisymmetric cross-section could be well approximated by modeling the acoustic radiation from a flat-plate turbulent boundary layer in an unconfined setting, after imposing similar freestream conditions and streamwise pressure gradients. The present results provide the basis for follow-on simulations involving reverberation effects inside the nozzle.

Acknowledgments

References

[1]Fedorov, A. V., "Receptivity of a High-Speed Boundary Layer to Acoustic Disturbances," *Journal of Fluid Mechanics*, Vol. 491, 2003, pp. 101–129.

(a) $z/\delta = 0$

(b) $z/\delta = 0.18$

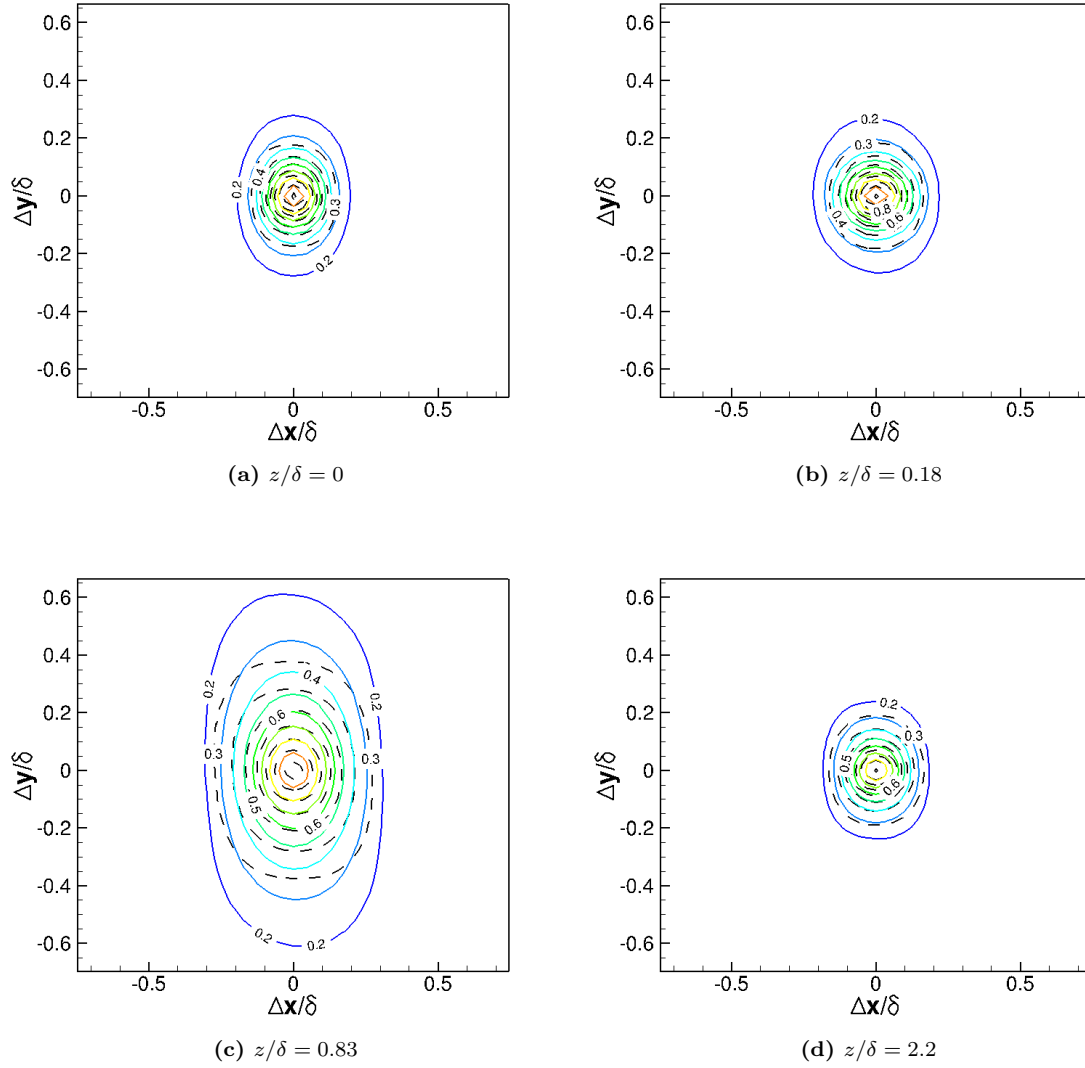**(c)** $z/\delta = 0.83$

(d) $z/\delta = 2.2$

Figure 11. Contours of constant streamwise-spanwise correlation coefficient of the pressure signal $C_{pp}(\Delta x, \Delta y)$ at selected heights for Case CylinderExpand (Colored solid line) and Case FlatPlate (Black dashed line). Contour levels vary from 0.2 to 0.9 with increments of 0.1.

American Institute of Aeronautics and Astronautics

(a) $z/\delta = 0$

(b) $z/\delta = 0.18$
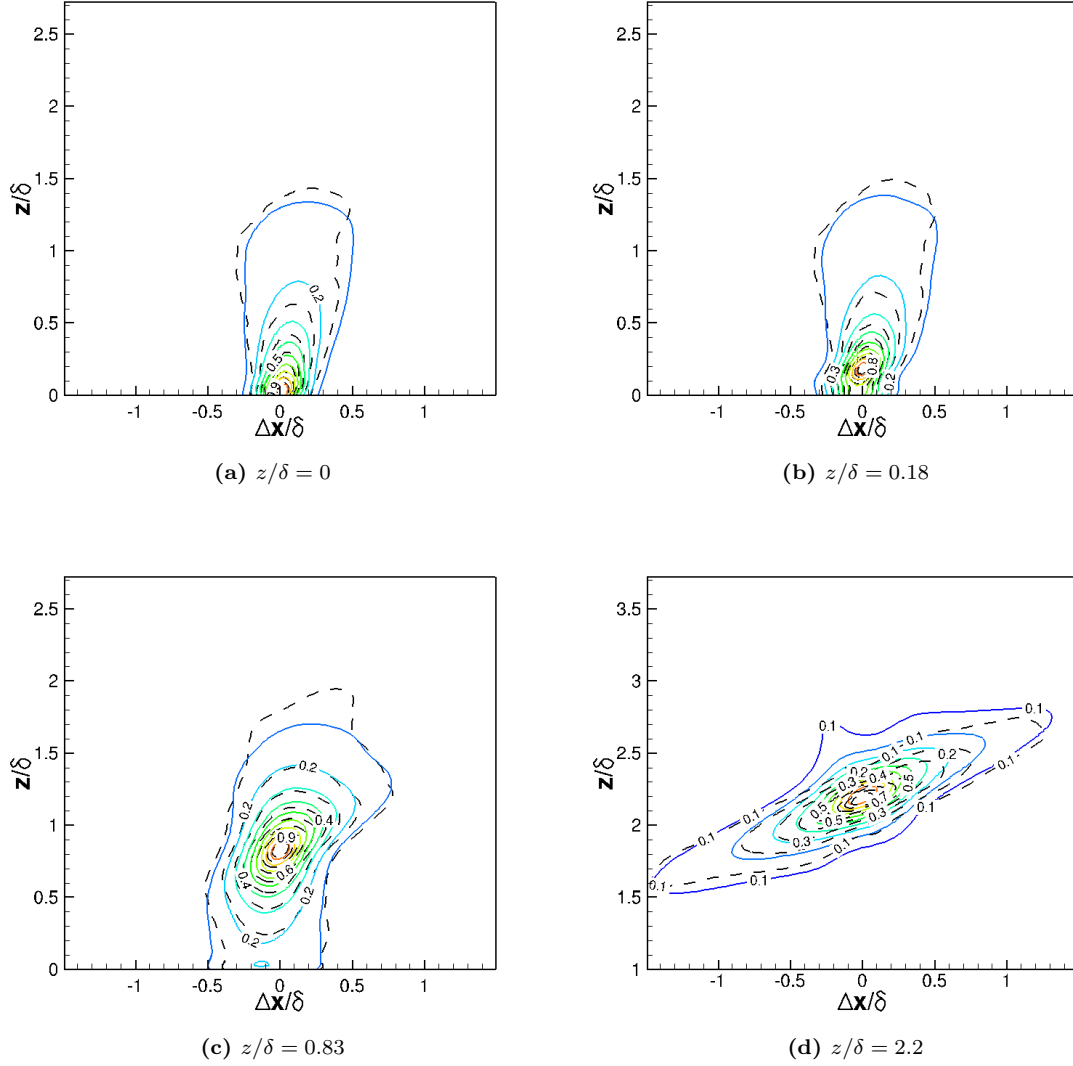
(c) $z/\delta = 0.83$

(d) $z/\delta = 2.2$

Figure 12. Contours of constant streamwise wall-normal correlation coefficient of the pressure signal $C_{pp}(\Delta x, z, z_{ref})$ at selected heights for Case CylinderExpand (Colored solid line) and Case FlatPlate (Black dashed line). Contour levels vary from 0.1 to 0.9 with increments of 0.1.

(a) $z/\delta = 0$

(b) $z/\delta = 0.18$

(c) $z/\delta = 0.83$

(d) $z/\delta = 2.2$

Figure 13. Contours of constant spanwise wall-normal correlation coefficient of the pressure signal $C_{pp}(\Delta y, z, z_{ref})$ **at selected heights for Case CylinderExpand (Colored solid line) and Case FlatPlate (Black dashed line). Contour levels vary from 0.2 to 0.9 with increments of 0.1.**
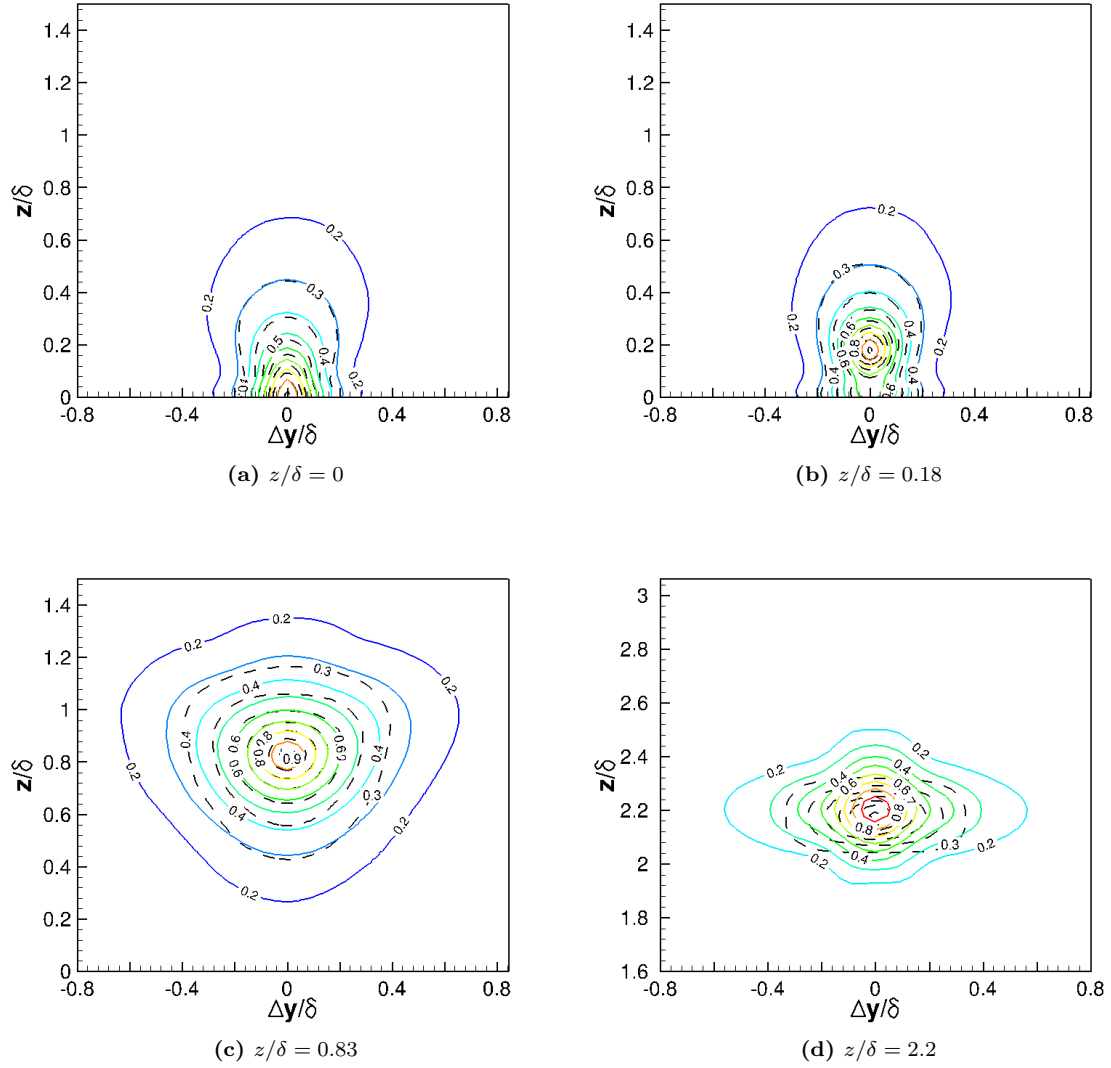
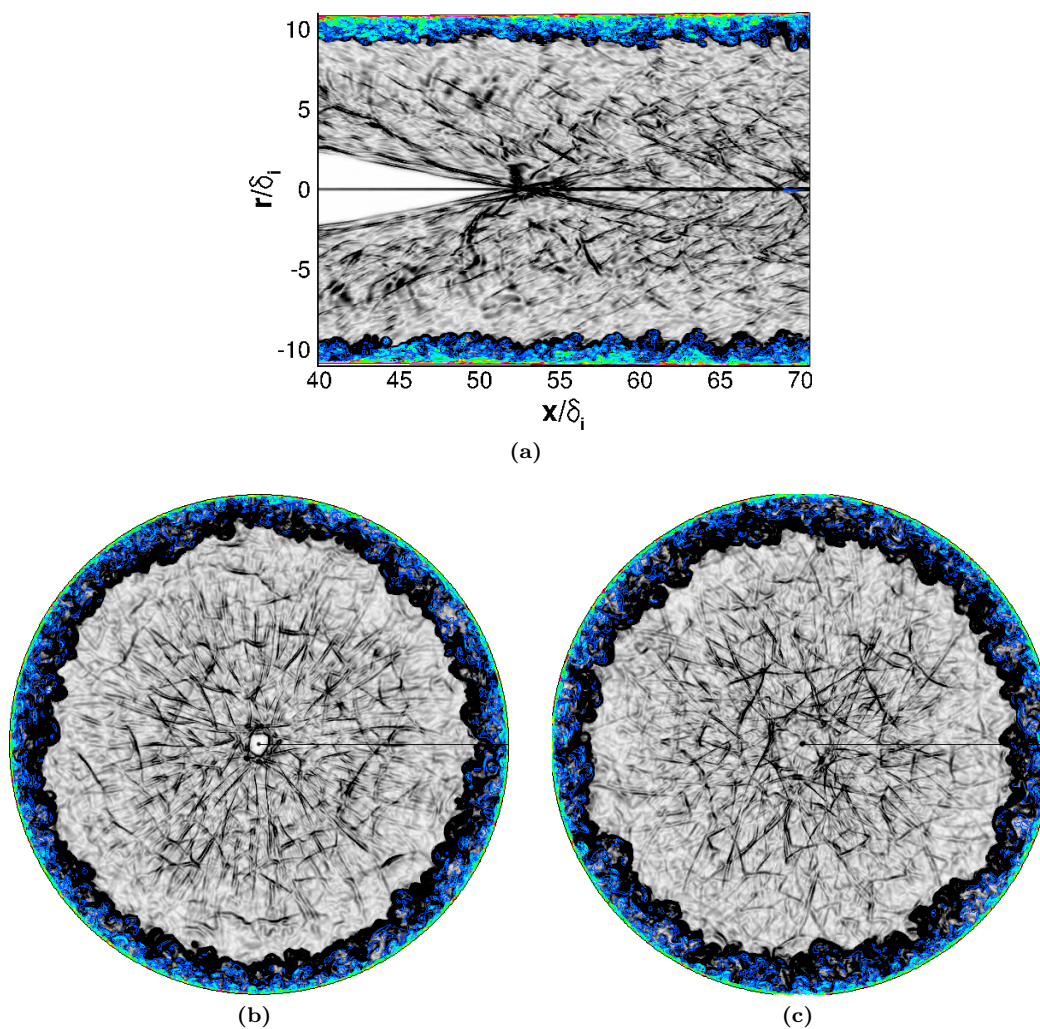American Institute of Aeronautics and Astronautics

Figure 14. Numerical Schlieren images of radiation wave in (a) a streamwise-radial plane between $40 < x/\delta_i < 70$, cross sections at (b) $x/\delta_i = 50$, and (c) $x/\delta_i = 60$. Contours are colored by the magnitude of vorticity.

American Institute of Aeronautics and Astronautics

[2]Zhong, X. and Wang, X., "Direct Numerical Simulation on the Receptivity, Instability, and Transition of Hypersonic Boundary Layers," *Annu. Rev. Fluid Mech.*, Vol. 44, 2012, pp. 527–561.

[3]Laufer, J., "Some Statistical Properties of the Pressure Field Radiated by a Turbulent Boundary Layer," *Physics of Fluids*, Vol. 7, No. 8, 1964, pp. 1191–1197.

[4]Donaldson, J. and Coulter, S., "A Review of Free-Stream Flow Fluctuation and Steady-State Flow Quality Measurements in the AEDC/VKF Supersonic Tunnel A and Hypersonic Tunnel B," AIAA Paper 95-6137, 1995.

[5]Schneider, S. P., "Effects of High-Speed Tunnel Noise on Laminar-Turbulent Transition," *Journal of Spacecraft and Rockets*, Vol. 38, No. 3, 2001, pp. 323–333.

[6]Duan, L., Choudhari, M. M., and Wu, M., "Numerical Study of Pressure Fluctuations due to a Supersonic Turbulent Boundary Layer," *Journal of Fluid Mechanics*, Vol. 746, 2014, pp. 165–192.

[7]Duan, L. and Choudhari, M. M., "Numerical Study of Pressure Fluctuations due to a Mach 6 Turbulent Boundary Layer," AIAA Paper 2013-0532, 2013.

[8]Duan, L. and Choudhari, M. M., "Analysis of Numerical Simulation Database for Pressure Fluctuations Induced by High-Speed Turbulent Boundary Layers," AIAA Paper 2014-2912, 2014.

[9]Borg, M. P. and Schneider, S. P., "Effect of Free-stream Noise on Roughness-Induced Transition for the X-51A Forebody," *Journal of Spacecraft and Rockets*, Vol. 45, No. 6, 2008, pp. 1106–1116.

[10]Wu, M. and Martín, M. P., "Direct numerical simulation of supersonic boundary layer over a compression ramp," *AIAA Journal*, Vol. 45, No. 4, 2007, pp. 879–889.

[11]Constantinescu, G. S. and Lele, S. K., "A Highly Accurate Technique for the Treatment of Flow Equations at the Polar Axis in Cylindrical Coordinates Using Series Expansions," *Journal of Computational Physics*, Vol. 183, 2002, pp. 165–186.

[12]Bogey, C., de Cacqueray, N., and Bailly, C., "Finite Differences for Coarse Azimuthal Discretization and for Reduction of Effective Resolution Near Origin of Cylindrical Flow Equations," *Journal of Computational Physics*, Vol. 230, 2011, pp. 1134–1146.

[13]Jiang, G. S. and Shu, C. W., "Efficient Implementation of Weighted ENO Schemes," *Journal of Computational Physics*, Vol. 126, No. 1, 1996, pp. 202–228.

[14]Taylor, E. M., Wu, M., and Martín, M. P., "Optimization of Nonlinear Error Sources for Weighted Non-Oscillatory Methods in Direct Numerical Simulations of Compressible Turbulence," *Journal of Computational Physics*, Vol. 223, No. 1, 2006, pp. 384–397.

[15]Williamson, J., "Low-Storage Runge-Kutta Schemes," *Journal of Computational Physics*, Vol. 35, No. 1, 1980, pp. 48–56.

[16]Martín, M., "DNS of Hypersonic Turbulent Boundary Layers. Part I: Initialization and Comparison with Experiments," *Journal of Fluid Mechanics*, Vol. 570, 2007, pp. 347–364.

[17]Duan, L., Beekman, I., and Martín, M. P., "Direct Numerical Simulation of Hypersonic Turbulent Boundary Layers. Part 3: Effect of Mach Number," *Journal of Fluid Mechanics*, Vol. 672, 2011, pp. 245–267.

[18]Duan, L., Choudhari, M. M., Li, F., and Wu, M., "Direct Numerical Simulation of Transition in a Swept-Wing Boundary Layer," AIAA Paper 2013-2617, 2013.

[19]Choudhari, M. M., Li, F., Duan, L., Chang, C.-L., Carpenter, M. H., Streett, C. L., and Malik, M. R., "Towards Bridging the Gaps in Holistic Transition Prediction via Numerical Simulations (Invited)," AIAA Paper 2013-2718, 2013.

[20]Touber, E. and Sandham, N. D., "Oblique Shock Impinging on a Turbulent Boundary Layer: Low-Frequency Mechanisms," AIAA Paper 2008-4170, 2008.

[21]Dhamankar, N. S., Martha, C. S., Situ, Y., Aikens, K. M., Blaisdell, G. A., and Lyrintzis, A. S., "Digital Filter-Based Turbulent Inflow Generation for Jet Aeroacoustics on Non-Uniform Structured Grids," AIAA Paper 2014-1401, 2014.

[22]Thompson, K. W., "Time Dependent Boundary Conditions for Hyperbolic Systems," *Journal of Computational Physics*, Vol. 68, No. 1, Jan. 1987, pp. 1–24.

[23]Huang, J., Zhang, C., and Duan, L., "Turbulent Inflow Generation for Direct Simulations of Hypersonic Turbulent Boundary Layers and their Freestream Acoustic Radiation," AIAA Paper 2016-3639, 2016.

[24]Eggels, J., Unger, F., Weiss, M., Westerweel, J., Adrian, R., Friedrich, R., and Nieuwstadt, F., "Fully developed turbulent pipe flow: a comparison between direct numerical simulation and experiment," *Journal of Fluid Mechanics*, Vol. 268, 1994, pp. 175–210.

[25]Duan, L., Choudhari, M. M., and Zhang, C., "Pressure Fluctuations induced by a Hypersonic Turbulent Boundary Layer," *Journal of Fluid Mechanics*, Vol. 804, 2016, pp. 578–607.